

Phenolic multiple kinetics-dynamics and discrete crystallization thermodynamics in amorphous carbon nanostructures for electromagnetic wave absorption

Received: 14 June 2024

Accepted: 19 November 2024

Published online: 28 November 2024

Jiaqi Tao¹, Kexin Zou¹, Jintang Zhou¹✉, Hongjing Wu²✉, Linling Xu³, Jin Wang⁴✉, Xuewei Tao⁵, Hexia Huang^{1,6}✉ & Zhengjun Yao¹✉

The lack of a chemical platform with high spatial dimensional diversity, coupled with the elusive multi-scale amorphous physics, significantly hinder advancements in amorphous electromagnetic wave absorption (EWA) materials. Herein, we present a synergistic engineering of phenolic multiple kinetic dynamics and discrete crystallization thermodynamics, to elucidate the origin of the dielectric properties in amorphous carbon and the cascade effect during EWA. Leveraging the scalability of phenolic synthesis, we design dozens of morphologies from the bottom up and combine with in-situ pyrolysis to establish a nanomaterial ecosystem of hundreds of amorphous carbon materials. Based on controlled discrete crystallization, nano-curvature regulation of spatial inversion symmetry-breaking structures, and surface electric field enhancement from multi-shell structures, the multi-scale charge imbalance triggers intense polarization. Both experiments and theories show that each scale is essential, which collectively drives broadband absorption (8.46 GHz) and efficient dissipation (−54.77 dB) of EWA performance. Our work on the amorphous nanostructure platform and the cascade effect can contribute to uncovering the missing pieces in amorphous physics and EWA research.

Since the advent of communication technology, the power flux density of electromagnetic radiation has exceeded natural levels by over 10^{18} times, establishing significant correlations with epidemiological and physiological responses as well as electronic device reliability^{1,2}. Although crystallography and computer science can guide electromagnetic wave absorption (EWA) material design to mitigate electromagnetic pollution, this is unsuitable for amorphous systems^{3–6}. On one hand, the short-range order and long-range disorder in the spatial

arrangement of amorphous units render inscrutable intrinsic properties^{7,8}. On the other hand, the lack of unified physical laws across multiple length scales in amorphous physics, an essential branch of condensed matter physics, further makes amorphous materials more mysterious⁹. Therefore, the truth about amorphous matter and its electromagnetic property manipulation is one of the most cutting-edge, intriguing, and challenging basic scientific topics at the intersection of condensed matter physics and materials science.

¹College of Materials Science and Technology, Nanjing University of Aeronautics and Astronautics, Nanjing, China. ²School of Physical Science and Technology, Northwestern Polytechnical University, Xi'an, China. ³School of Electronic Science and Engineering, Nanjing University, Nanjing, China. ⁴College of Electronic and Optical Engineering & College of Flexible Electronics (Future Technology), Nanjing University of Posts and Telecommunications, Nanjing, China. ⁵School of Materials Science and Engineering, Nanjing Institute of Technology, Nanjing, China. ⁶College of Energy and Power Engineering, Nanjing University of Aeronautics and Astronautics, Nanjing, China. ✉e-mail: imzjt@126.com; wuhongjing@nwpu.edu.cn; jin@njupt.edu.cn; huanghexia@nuaa.edu.cn; yaozj1921@126.com

Amorphous carbon is an apt research object, as it can offer abundant allotropes with different properties through flexible carbon atom hybridization and morphological designs^{10,11}. In terms of carbon atom hybridization, the competition between sp^2 and sp^3 hybridization modes exhibits a vague compromise principle, granting amorphous carbon unparalleled dielectric flexibility^{12–14}. According to the temperature-dependent hopping conductivity model established by Tian et al., the astounding billion-fold nonlinear physical changes are induced by the content and distribution of sp^2 - sp^3 hybridized domains¹⁵. In terms of morphological design, the construction of unique structures (e.g., hollow^{16–18}, porous^{19–21}, bowl-shape^{22,23}, etc) can modulate the physical properties of amorphous carbon, including the introduction of air to adjust impedance^{24–26}, improvement of light-weight properties to enhance equivalent media parameters^{27,28}, and the provision of irregular surfaces to increase scattering sites^{29,30}. Despite achievements that have been made independently at the atomic and morphological levels, unfortunately, the correlation between these two aspects has been neglected. Recently frontier studies attribute the scaling effect in dynamic glass-transitioning to the inter- and intra-chain phase separation interactions, deepening the interdisciplinary and cross-scale nexus between condensed matter physics and chemistry³¹. Inspired by this, we argue that the current amorphous EWA research lacks a necessary jigsaw, preventing the fragmented studies from forming a cohesive whole. Because the functionality of EWA essentially stems from complex collective behaviors across different scales^{32,33}, similar to the large and small gears in a mechanical system, which appear separate but are interconnected.

Up to now, our limited understanding of boundaries and internal mechanisms in different spatial dimensions has obscured the beauty and clearness of the entire EWA amorphous system^{34,35}. To overcome this challenge, we need to address two crucial issues: i) Develop a cross-scale platform with high spatial dimension diversity to bridge the gap between different scales, connecting mechanisms at the unit scale to behaviors in macroscopic systems. ii) Through this platform, interpret the complex collective behaviors in amorphous systems and establish a general principle that effectively connects different disciplines across different levels, thereby expanding the applicability of amorphous science in precise electromagnetic control and the development of novel characteristics.

In this work, starting from the phenolic synthesis dynamics, novel kinetic-dynamics regulation methods and multi-shelling techniques are progressively introduced to develop a phenolic nanostructure library, encompassing 23 nano-shapes, including spatial inversion symmetry (SIS) and spatial inversion symmetry-breaking (SISB) structures. Then, we obtain 330 phenolic-derived amorphous carbon through in-situ pyrolysis and study the contributions of atomic configuration, nano-curvature interface, and microstructure. The results indicate that dielectric polarization initially originates from discrete sp^2 domains, bringing conjugated-nonconjugate interface polarization. This polarization is amplified and accumulated multiple times due to the nano-curvature field effect of SISB structures and the surface electric field enhancement effect of multi-shell structures, ultimately achieving broadband absorption exceeding 8 GHz. Meanwhile, we propose a cross-scale cascade effect to explain this multi-scale dielectric coupling phenomenon and validate this indispensable progressive relationship based on a rich database.

Results

Phenolic Nanostructures

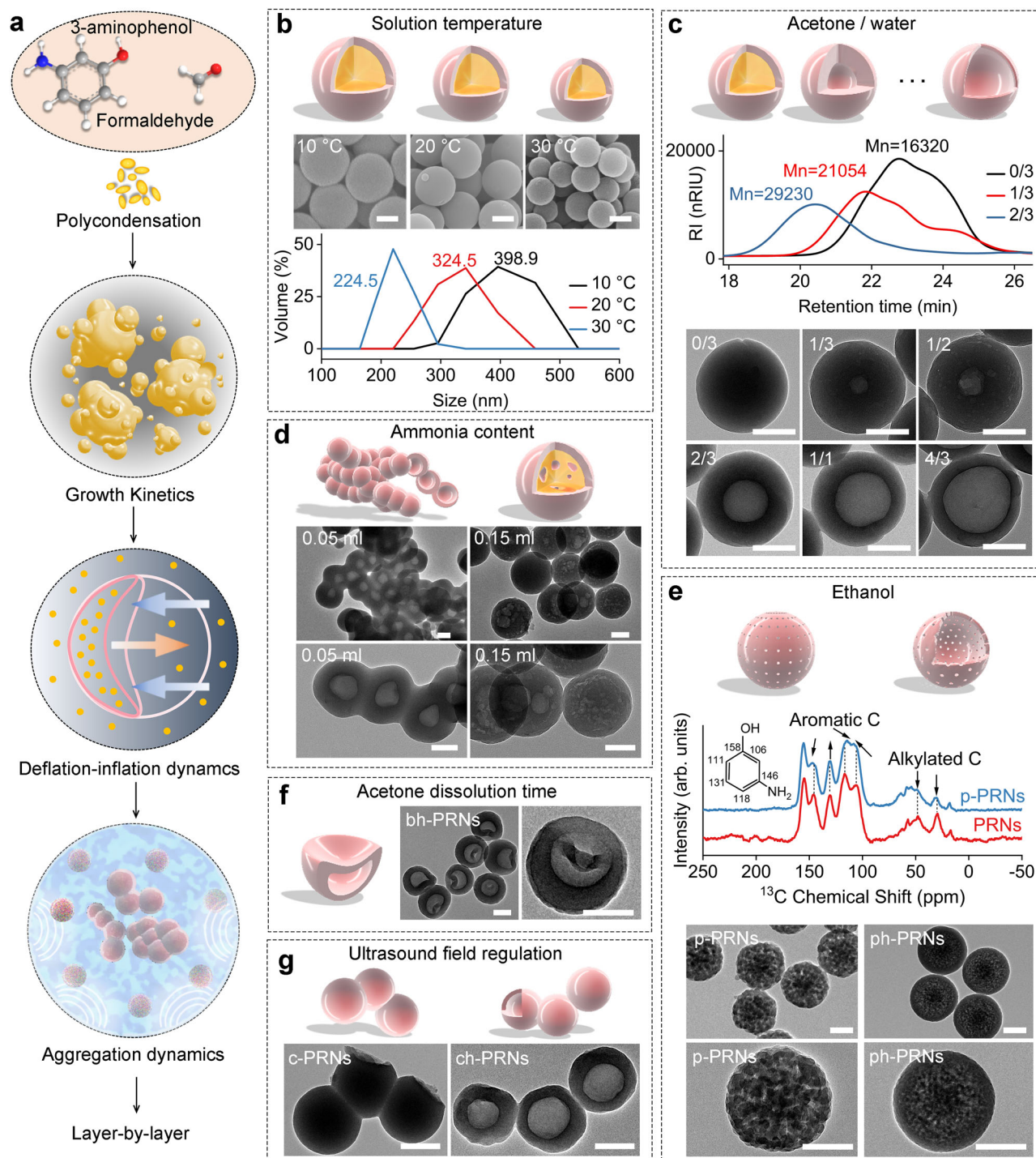
Through the high activity of phenol, the strong electron affinity of phenolic hydroxyl groups or the reduction ability of aldehyde, the morphology can be designed on the nano-micro scale³⁶, resulting in a series of phenolic resin nanoparticles (PRNs) with exquisite structure. All the regulation is based on the Polycondensation of 3-aminophenol and formaldehyde in an ammonia solution, which

involves one or more dynamics and kinematics (Fig. 1a and Supplementary Fig. S1).

To finely manipulate morphology, we explore pivotal phenolic growth kinetics under varying experimental conditions, including temperature, organic etching solvents, and ammonia concentrations. Typically, the synthesis of PRNs involves nucleation, growth, and aging stages. Through systematic temperature augmentation (10, 20, 30 °C), we observe an expedited nucleation rate coupled with diminished particle dimensions (Fig. 1b). To ensure consistency, comparative experiments are conducted at a fixed 20 °C. Notably, phenolic aging occupies most of the reaction time, which leads to uneven molecular weight of individual nanospheres (Supplementary Fig. S2). The central region of PRNs is limited contact with ammonia, resulting in lower polymerization than the surface. This invisible gradient distribution of polymerization degree inspires us to fabricate hollow PRNs (h-PRNs) by an appropriate solvent. We have evaluated various organic solvents and realize that only acetone can establish impressive correlations with the phenolic molecular weight or hollow structure (Fig. 1c and Supplementary Fig. S3). Specifically, elevating the acetone/water ratio enables the retention of higher molecular weight fractions, thereby facilitating greater hollow degrees. Furthermore, we confirmed the effect of ammonia concentration on the molecular weight gradient distribution and the effectiveness of acetone (Fig. 1d). At low ammonia concentrations, phenolic growth is sluggish, leading to severe nanoparticle aggregation, while excessively high concentrations result in disordered molecular weight distributions. Despite the appearance of cavities post-acetone etching, they are not an ideal hollow structure.

Based upon findings of phenolic growth kinetics on nanostructures formation, we then tweak orthogonal experiments to develop mutated hollow structures by modify the phenolic growth kinetics or introduce new dynamics.

1. The porous hollow structure is derived from ethanol-modified phenolic growth kinetics (Fig. 1e). Although ethanol cannot dissolve high-polymerized phenolic, it can participate in the early condensation nucleation stage to dissolve low-polymerized part with molecular weights below 700 (Supplementary Fig. S4). Solid-state nuclear magnetic resonance (ssNMR) shows that ethanol cleaves alkylated carbon bonds, aromatic C-C bonds, and aromatic C-N bonds on the molecular chains, generating hydroxymethyl derivatives³⁷. This ethanol-assisted chemical bond breakage-regeneration behavior is not extensive, confined to local regions of approximately 10–20 nm, see the porous PRNs (p-PRNs) (Supplementary Fig. S5). Since ethanol does not interfere with the polymerization degree gradient, we can still construct hollow structures using acetone, see the porous hollow PRNs (ph-PRNs).
2. The Bowl-shaped hollow structure is constructed using inflation-deflation dynamics (Fig. 1f). Acetone, as a sensitive phenolic etchant, can completely remove the low-polymerized core in a short time. However, this creates a transient large pressure difference between the inside and outside of the hollow shell. The external pressure is higher than the internal, causing the PRNs to collapse like a deflated basketball, resulting in a complete bowl-shape without a cavity (Supplementary Fig. S6). This state cannot be maintained for a long time. The higher concentration of low-polymerized species inside leads to spontaneous solvent penetration, so as to reduce concentration and pressure differences (Supplementary Fig. S7). This infiltration mechanism drives the inflation process and produces bowl-shaped hollow PRNs (bh-PRNs). Furthermore, the difference in geometry and curvature radius on surfaces affects the interaction and molecular diffusion behavior between low-polymerized species and the surface³⁸. It promotes asymmetric growth of the shell, manifesting as thickening on the positive curvature surface and thinning on the negative curvature surface, until inflation forms a hollow



structure. The dynamic clarity of the solution suggests this process (Supplementary Fig. S8).

- The short chain-like hollow structure is constructed by utilizing ultrasound to modulate interfacial polymerization dynamics (Fig. 1g). The strong ultrasound collapses cavities and bubbles in the solution, generating microjets with strong impact forces that propel solution vibration and nanoparticle movement^{39,40}. The liquid shear flow imposes shear stress on the nanoparticle surfaces, thereby disrupting particle aggregation. Meanwhile, ultrasonic high-frequency vibration waves directly act on the nanoparticle surfaces, causing relative displacement between particles and surrounding solution molecules, reducing interfacial aggregation dynamics, and promoting nanoparticle dispersion.

Previous samples underwent ultrasonic treatment at a 40 KHz frequency, equivalent to 4×10^4 impacts per second, resulting in good dispersion. Conversely, reducing the ultrasound frequency allows PRNs to recover weak van der Waals forces and form mild aggregations. This reverse application of interfacial polymerization kinetics facilitates the construction of short chain-like PRNs (c-PRNs) and short chain-like hollow PRNs (ch-PRNs). The difference in van der Waals interfacial forces is corroborated by periodic optical contrast (Supplementary Fig. S9).

Interestingly, PRNs can serve as seeds to provide growth and deposition sites for phenolic aldehydes obtained through subsequent polycondensation reactions (Supplementary Fig. S10). This inspires us

Fig. 1 | Multiple kinetics-dynamics engineering of phenolic nanostructures.

a Schematic diagrams of phenolic growth kinetics, inflation-deflation kinetics, and interfacial polymerization kinetics. Yellow dots represent phenolic small-molecule polymers, while yellow irregular shapes denote the transition from small-molecule clusters to large-molecule phenolic aggregates. Pink spheres represent phenolic large-molecule polymers. Blue arrows illustrate the process of particle deflation and depression, whereas orange arrows depict the phenomenon of particle inflation and expansion. The ultrasonic environment is indicated by the blue background, complemented by white lines that symbolize the ultrasonic waves. **b** Changing the solution temperature modulates the phenolic growth kinetics. Scanning electron microscopy (SEM) images and dynamic light scattering spectra of phenolic resin nanoparticles (PRNs) obtained at different solution temperatures. The inside yellow spheres indicate phenolic small-molecule polymers that can be etched by acetone. **c** Acetone as a low molecular polymer etchant to verify the gradient polymerization degree due to phenolic growth kinetics. The gel permeation chromatography and transmission electron microscope (TEM) images of PRNs etched with different acetone/water ratios. Mn is number-average molecular

weight. **d** Too high or too low a concentration of ammonia can disrupt phenolic growth kinetics. TEM images of different ammonia content. Irregular yellow kernels indicate that it is not all small-molecule polymers, which acetone cannot etch completely. **e** Phenolic growth in an ethanol solution results in the formation of porous structures due to localized early dissolution of small molecule polymers. Solid state nuclear magnetic resonance ^{13}C spectra obtained from ethanol-modified phenolic growth kinetics, and TEM images of porous PRNs (p-PRNs) and porous hollow PRNs (ph-PRNs). **f** The rapid etching action of acetone resulted in rapid shrinkage of the particles and slow expansion over the next 30 minutes. Etching time-dominated modulation of inflation-deflation dynamics achieves bowl-to-spherical transient capture. TEM images of bowl-shaped hollow PRNs (bh-PRNs) obtained from inflation-deflation dynamics. **g** Ultrasonic power modulates the interfacial polymerization kinetics of phenolics. TEM images of short chain-shaped PRNs (c-PRNs) and short chain-shaped hollow PRNs (ch-PRNs) obtained from interfacial polymerization dynamics. The scale of above SEM images and TEM images is 200 nm.

to use the Layer-By-Layer process to achieve the free superimposition of multiple kinetics and dynamics, and construct multi-shell structures⁴¹. For instance, PRNs are first uniformly dispersed in the next set of ammonia aqueous solutions, and then a second shell is obtained through similar experimental operations, including phenolic condensation, acetone etching (volume and time), and other treatments (ethanol and ultrasound power). Theoretically, the corresponding shell number can be obtained by repeating the above process several times (Fig. 2a). We have processed the SIS structure (hollow and porous hollow) and SISB structure (bowl-shaped hollow and short chain-shaped hollow) into multiple shells and labeled them accordingly (Fig. 2b–e). Specific synthesis parameters are summarized in Supplementary Table S1.

The above 23 structures with different morphologies and shell numbers show an evolving nanoart, sufficient to support the follow-up valuable EWA analysis, including the effects of atomic configuration, SIS/SISB structure, shell numbers on the dielectric properties, and their synergistic effect.

Thermodynamic regulation

The atomic configuration transformation process of phenolic-derived amorphous carbon is investigated through In-situ thermogravimetry-differential scanning calorimetry-mass spectrometry, fourier transform infrared spectroscopy, and x-ray photoelectron spectroscopy. As shown in Fig. 2f, before 600 °C, phenolic long chains thermally crack into short chains (stage 1), and these short chains then undergo carbonization (stage 2), causing residual C atoms to gradually aggregate and form discrete sp^2 - sp^3 hybridized domains. Beyond 600 °C, a dehydrogenation and cyclization reaction (stage 3) occurs, accompanied by a significant endothermic phenomenon and a disruptive transformation in molecular conformation. With continuous thermal stimulation, unsaturated C atoms at the edges began to interconnect, merging the discrete disordered domains and eliminating a significant number of unpaired edge electrons. As demonstrated in Supplementary Fig. S11, the conjugated structures of aromatic rings undergo intense motion, enhancing vibrational energy, which leads to a red shift in the Ar-H peak, from 751 cm^{-1} to 726 cm^{-1} . Additionally, atoms and groups vibrate, rotate, or detach from their original structures (Supplementary Fig. S12), disrupting the original stable overlap of atomic orbitals and rearranging the electrons within the bonds. This transformation manifested in the conversion of non-conjugated sp^3 -C to more stable, lower internal energy, and more evenly spaced conjugated sp^2 -C (Fig. 2g). Notably, the rearrangement of carbon atoms hardly resulted in micro deformation or element segregation (Fig. 2h and Supplementary Figs. S13–S14), which facilitates the establishment of a clear multi-scale classification of complex collective

behaviors in amorphous physical systems without having to worry about their confusion due to pyrolysis.

We have also validated the controllable crystallization of the amorphous carbon. High-resolution TEM images and diffuse halos reveal (Fig. 2i and Supplementary Fig. S15) that the carbon lattice is long-range disorder, indicating the overall amorphous nature of the material. However, at 700–1000 °C, short-range ordered lattice fringes of 0.36 nm (highlighted by yellow regions) from the (002) graphite phase are captured at the shell edges. As the temperature increases, graphite microcrystals grow and become continuous. This improved crystallization is also identified in the XRD spectra (Supplementary Fig. S16). Besides, we compare the sp^2 and sp^3 bonding states of carbon atoms. By deriving Auger electron spectroscopy and comparing the kinetic energy differences between binding energy extrema, the sp^2 bonding content is calculated to be 7.07, 23.2, 32.3, 37.4, and 43.4 at% (Supplementary Fig. S17). The reliability of this trend is further corroborated by the Gaussian fitting data of the C1s spectra and the I_D/I_G ratio from Raman spectra (Supplementary Fig. S18–19 and Table S2). These characterizations collectively demonstrate that elevated temperatures promote the growth and interconnection of discrete graphite microcrystals within the sp^2 - sp^3 hybridized carbon framework.

Sources of dielectric properties

For 2–18 GHz EWA research, there are at least five orders of length scale differences between microwave wavelengths (16.67–150 mm) and our nanomaterials, which requires fully considering the complexity of multi-scale and interdisciplinary. Based on 330 sets of electromagnetic parameters, we have found that the pyrolysis temperature significantly affects the dielectric properties of amorphous carbon (Supplementary Figs. S20–S41). Taking the triple-shell hollow PRNs (mh-PRNs-2) derived amorphous carbon as a representative, the group with a high sp^2 content exhibits more sensitive electric field response characteristics and stronger dielectric loss capabilities (Fig. 3a). To gain a deeper understanding of dielectric properties, a nonlinear fitting of the modified Debye relaxation using the least squares method is conducted⁴². The results indicate that both the conductivity loss (ϵ_c'') and polarization loss (ϵ_p'') are enhanced (Fig. 3b).

The hybrid orbital theory sheds light on the microscopic origin of ϵ_c'' (Fig. 3c). During crystallization, parallel $2p_z$ orbitals of adjacent C atoms form π bonds, and six C atoms create a delocalized large π bond (π_6^6), possessing a weak electronic binding force. The formation of more sp^2 bonds liberates more delocalized π electrons from $2p_z$ orbitals (Fig. 3d), enhancing the carrier concentration. This is evidenced by the reduced electron-hole recombination rate in the steady-state photoluminescence spectra (Supplementary Fig. S42). Additionally, the continuous π_6^6 provides a high-speed channel for long-range

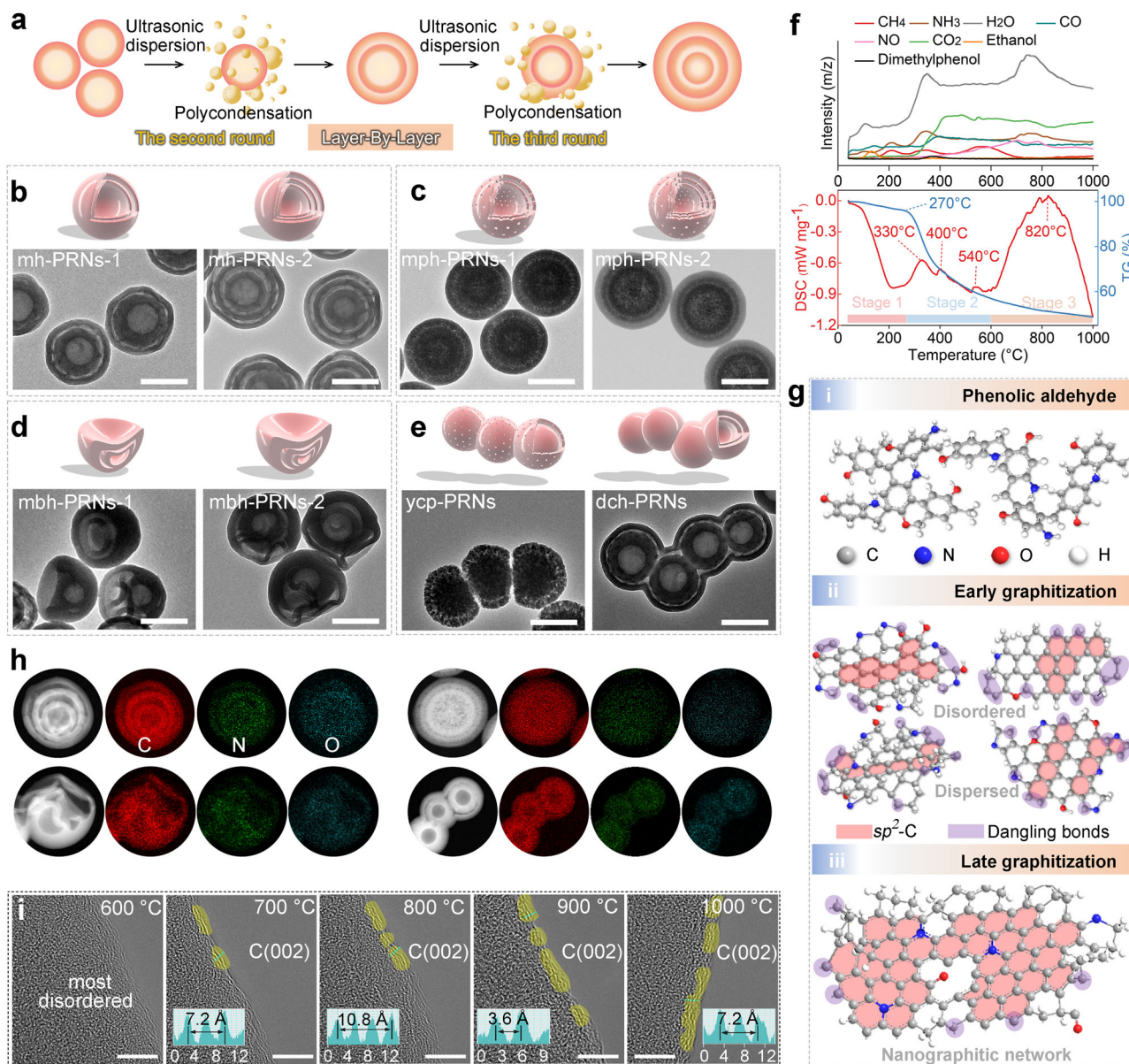


Fig. 2 | Multi-shelling and thermodynamic modulation of PRNs series. **a** The multi-shelling schematic. The red is indicative of the large-molecule segment, whereas the yellow denotes the small-molecule segment. **b** TEM images of double-shell hollow PRNs (mh-PRNs-1) and triple-shell hollow PRNs (mh-PRNs-2). **c** TEM images of double-shell porous hollow PRNs (mph-PRNs-1) and triple-shell porous hollow PRNs (mph-PRNs-2). **d** TEM images of double-shell bowl-shaped hollow PRNs (mbh-PRNs-1) and triple-shell bowl-shaped hollow PRNs (mbh-PRNs-2). **e** TEM images of yolk-shell short chain-shaped porous PRNs (ycp-PRNs) and double-shell short chain-shaped hollow PRNs (dch-PRNs). The scale of TEM images is

400 nm. **f** In-situ thermogravimetric-mass spectrometric-differential scanning calorimetry was used to document the thermodynamic behavior of phenolic aldehydes from room temperature to 1000 °C. **g** Schematic representation of the atomic configuration transformation of phenolic-derived amorphous carbon. **h** Elemental mapping images of phenolic-derived amorphous carbon with different multi-shell structures. Red is element C, green is element N, blue is element O. **i** High-resolution TEM images of mh-PRNs-2 crystallized at different temperatures, taken with a double spherical aberration-corrected TEM. The scale of High-resolution TEM images is 5 nm.

charge migration, reducing the energy barrier (Fig. 3e). Consequently, the samples exhibit conductivity spanning 6 magnitude orders (Fig. 3f). Undoubtedly, conductivity determines the ϵ_c'' value, corresponding to the free carrier contribution described by the Drude model⁴³. However, conductivity exceeding a threshold generates a strong induced current and reflects electromagnetic waves.

The microscopic origin of ϵ_p'' stems from the unusual conjugate-nonconjugate interface polarization, rather than functional groups or heteroatoms (Supplementary Figs. S11, 12 and Tables S3, S4). Unlike traditional crystalline heterogeneous interfaces, the heterophase Interface in amorphous carbon have often been neglected in previous

EWA studies^{26,44,45}. Theoretically, the delocalization of π electron clouds in conjugated structures relies on continuous π^6 . The different sizes and dispersities of sp^2 domains lead to diverse distributions of π electron clouds. Through density functional theory (DFT) calculations of Mulliken charge values and differential charge densities (Fig. 3g and Supplementary Fig. S43a, b), we found that charges tend to concentrate in sp^2 domains, with the relationship of corner state>edge state>bulk state. This indicates that the conjugate-nonconjugated interface can trap charges in alternating electromagnetic fields, resulting in the generation of space-charge regions and built-in electric fields, which subsequently induce micro-interface polarization.

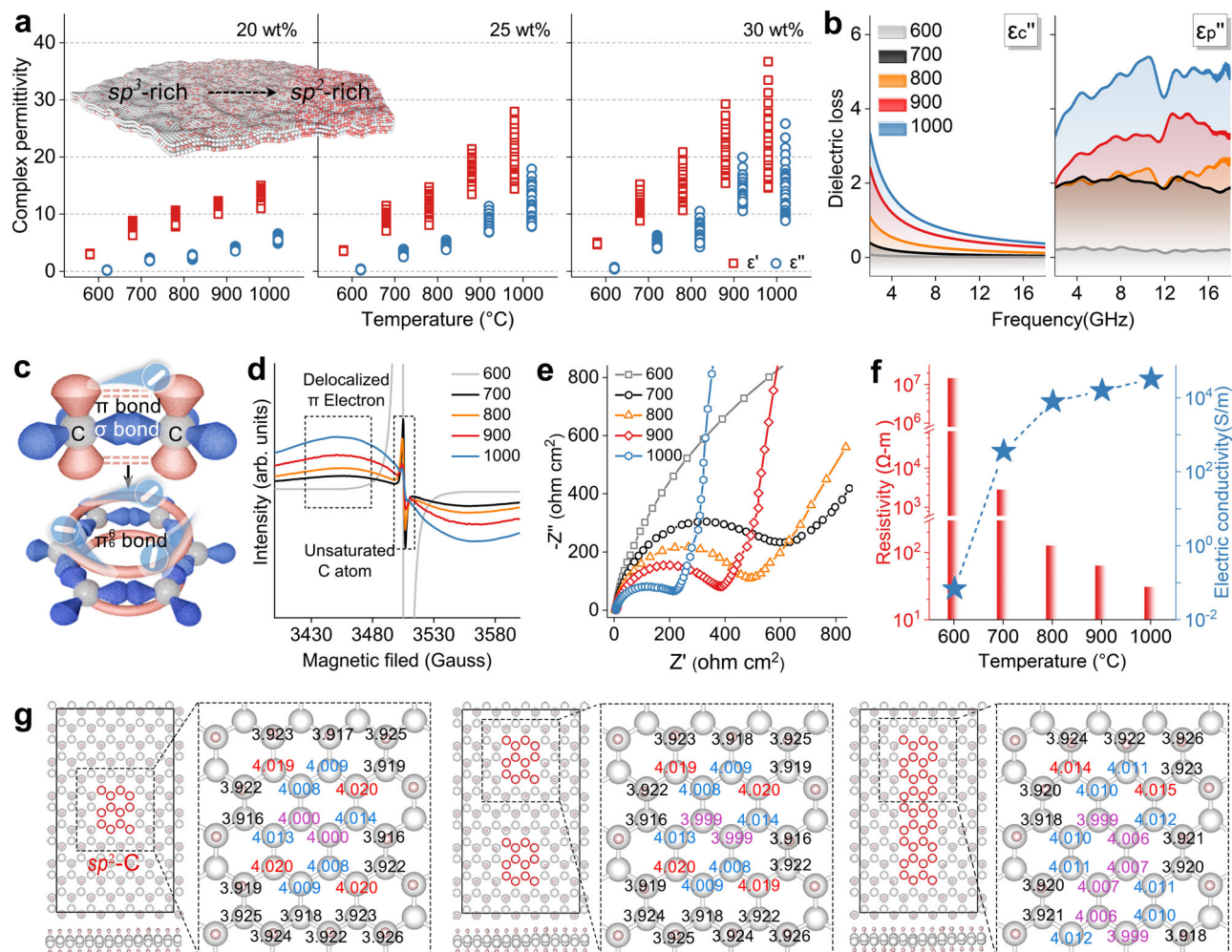


Fig. 3 | The relationship between pyrolysis parameters and dielectric properties. **a** Complex permittivity measured in 20, 25, and 30 wt% continuous dielectric frames. The upper left inset indicates the increase in sp^2 content with increasing pyrolysis temperature. **b** The imaginary part dielectric constant is fitted with 20 wt % filling, including conductivity loss (ϵ_c'') and polarization loss (ϵ_p''). **c** Schematic representation of the carbon sp^2 hybridization mode and electrical properties. The red orbitals are π -bonds and the blue orbitals are σ -bonds. The six π -bonds form

into one π^*_6 bond. **d** Results of electron paramagnetic resonance for amorphous carbon. **e** Results of electrochemical impedance spectroscopy for amorphous carbon. **f** The resistance measurements result by the four-probe method. **g** Mulliken charge calculations by density-functional theory (DFT) for sp^2 - sp^3 hybridization models with different sp^2 bond distributions. The red, blue, and purple numbers indicate the electrons in the corner state, edge state, and bulk state in the sp^2 region, respectively.

This interfacial loss contributes to high ϵ_p'' without reflecting electromagnetic waves^{46,47}.

An important point is that the effective contribution of microscopic polarization is not solely determined by the size of π electron clouds, but also closely related to discrete states of sp^2 domains. According to the ssNMR test (Supplementary Fig. S44), the higher sp^2 bonds dispersion is observed at 600–700 °C. Usually, the higher dispersibility of sp^2 bonds, the weaker interaction between π electron clouds, leading to less radio-frequency radiant energy consumption, making the sp^2 peak closer to the low chemical shift. The distinction to be made is that there are too few sp^2 bonds at 600 °C to form obvious sp^2 domains (Fig. 2i) and interface polarization. The density of states shows that the increase in discrete sp^2 domains does not significantly narrow the bandgap, whereas continuous sp^2 domains do (Supplementary Fig. S43c). Meanwhile, the discrete sp^2 domain tends to adjust the local electrostatic potential in the direction of arrangement rather than omnidirectional, which aggravates the non-uniform distribution of charge (Supplementary Fig. S43d). Although high concentrations of π^*_6 bonds enhance dielectric loss, the maximum sp^2 domains dispersion leads to the highest degree of charge

localization or deviation, resulting in ϵ_p'' increasing rapidly and ϵ_c'' increasing slowly. As evident from the dielectric fitting results (Supplementary Fig. S45 and Table S5), the ϵ_p'' of mh-PRNs-2 (700 °C, 20 wt%) is even dozens of times higher than ϵ_c'' , covering the X and Ku bands. We infer that the conjugate-nonconjugate interface polarization induced by discrete microcrystals in the amorphous system is the original of dominant dielectric loss, highly conducive to broadband absorption.

Further, we analyze the impact of morphology on polarization, including nano-curvature surface, spatial inversion symmetry degree, and multi-shell structures. Firstly, charges are more likely to gather in the positive curvature surface according to the Gaussian mathematical derivation (Supplementary Fig. S46). We have constructed conjugate models with different curvatures (≥ 0) and compared their effects on charge distribution (Fig. 4a). Obviously, each position of a flat model with zero curvature has the same charge distribution, so there is no electron density difference. In contrast, there is a charge density difference between the other two positive curvature models, which increases with the increase of curvature. This means that the larger the curvature, the more severe the charge imbalance, which enhances the

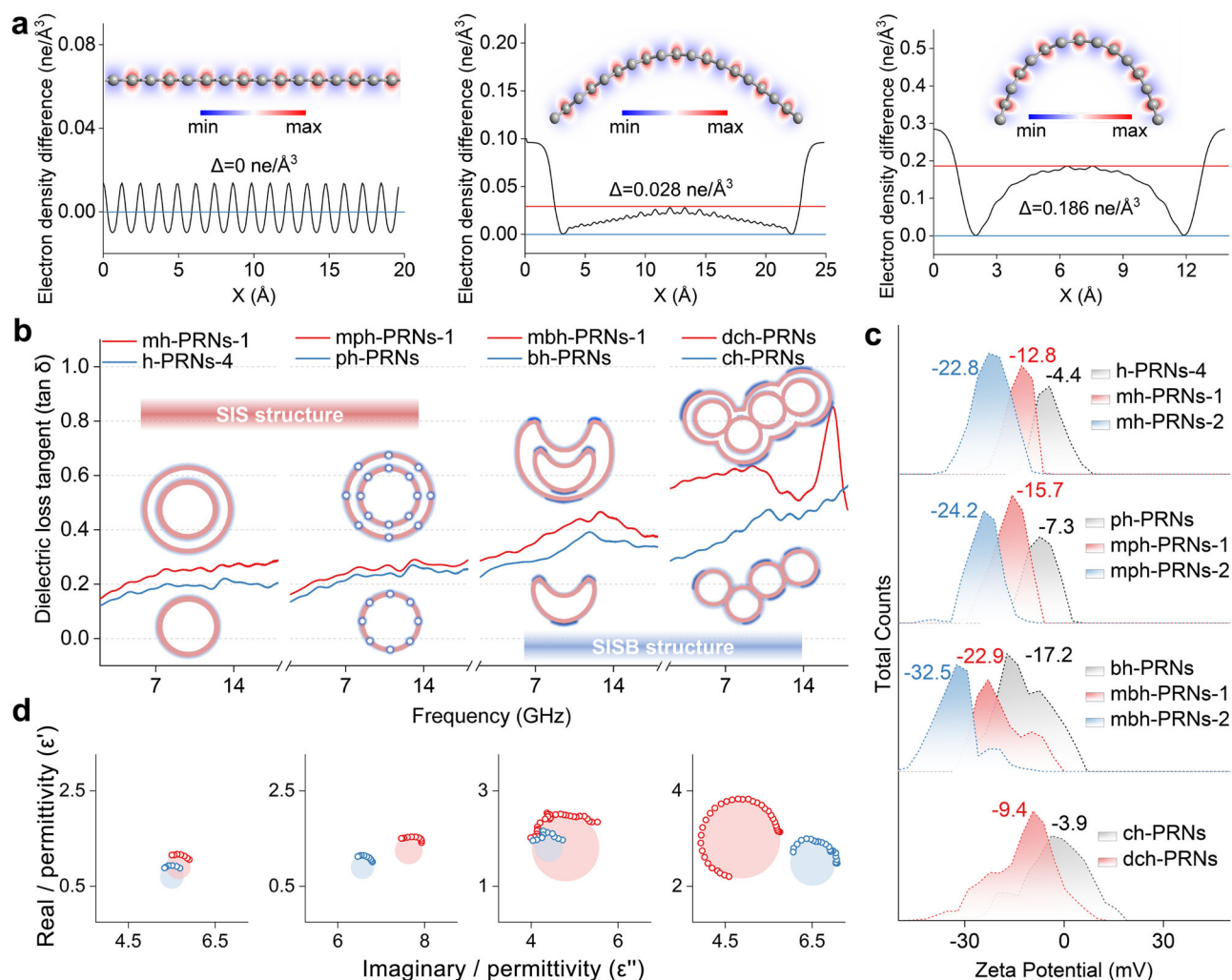


Fig. 4 | Effect of micromorphology on the dielectric loss. **a** Calculation of electron density difference for different curvature models averages over the plane spanned by the two other axes. The inset is a cross-section of the corresponding electron density difference distribution. Δ is the electron density difference from the center to the edge of the model. **b** Dielectric loss capacity for spatial inversion symmetry (SIS) structures and spatial inversion symmetry-breaking (SISB) structures in different shell numbers. The blue circles in the hollow porous schematic

refer to mesopores in the shell layer and regions where electrons tend to cluster. The blue lines in the bowl- and chain-shaped structures also indicate regions where electrons tend to cluster. **c** Zeta potential characterizes the effect of shell numbers on the surface electric field in hollow structures, porous hollow structures, bowl-like hollow structures, and short chain-like hollow structures. **d** The Cole-Cole curve of samples with the color corresponding to the icon of **b**. Shading indicates the extent of the Cole-Cole relaxation circle.

local electric field, similar to the tip effect⁴⁸. As shown in Fig. 4b, the dielectric loss capacity ($\tan\delta$) of hollow materials is enhanced by porous, bowl-like, and short chain-like morphologies, due to their local large curvature interface. Among them, a representative example is the bowl-shaped hollow structure. According to the equivalent medium theory, the hollow depression will reduce the volume, thus reducing the conductance loss. However, the $\tan\delta$ value increases, which indicates that the polarization loss has been greatly enhanced, masking other unfavorable factors. Therefore, this nano curvature-induced field effect triggers charge redistribution at the nanoscale, promoting conjugate-nonconjugate interface polarization on positively curved surfaces.

The final benefit of the nano curvature-induced field effect is magnified by the SISB structure and the multi-shell structure. Through more careful comparison, the porous morphology, classified as an SIS structure, exhibits less charge imbalance at the micrometer scale than the other SISB variants. This may be because the curvature difference caused by porosity is centrosymmetric on a larger scale. To get evidence, we characterize the surface potential properties by Zeta

spectroscopy⁴⁹. As depicted in Fig. 4c, the SIS structure exhibits a single narrow Zeta peak, while the SISB structure has multiple overlapping broad peaks, indicating a more extensive uneven surface charge distribution in the SISB structure. Combined with the higher $\tan\delta$ of the SISB structure, it can be concluded that dielectric loss depends on multi-scale charge imbalance, rather than a single scale. Besides, the multi-shell structure increases the surface potential of the sample and sharpens the main peak, suggesting that multi-shelling strategies facilitate enhanced surface electric fields and amplified charge imbalance in the SISB structure. Consequently, in multi-shell SISB structures, the large positive curvature surface, which is not arranged in a centrosymmetric manner, promotes the concentration of the induced charges. This enables the selective amplification of the surface electric field and enhances the polarization relaxation at the already existing conjugate-nonconjugate interface, leading to more efficient dissipation of electromagnetic waves. The evolution of several micro-nano-morphologies (hollow, porous hollow, bowl, and short chain) from single-shell to double-shell makes the Cole-Cole curves undergo different degrees of changes (Fig. 4d), i.e., the relaxation

circle of the SISB structure gets significantly enlarged while the SIS structure does not, proving the above reasoning.

So far, the interactions between the different scale parameters of EWA amorphous systems gradually show a cascade effect (i.e., chain reactions of internal mechanisms in different spatial dimensions), rather than just mere superposition. The further discussion to illustrate the importance of cascade effects on dielectric properties and EWA as follows:

1. Atomic configuration is the initial origin of dielectric properties and is intimately related to the effectiveness of following morphology modulation. The content and type of functional groups and heteroatoms are only controlled by graphitization temperature, rather than the morphology and multi-shell structure (Supplementary Figs. S11, 12, S47, and Tables S3, S4). As the temperature increases, the graphite N remains constant and the other polar groups (-OH, C-O, C=O, pyridine N, pyrrole N, etc.) decrease, implying that the conductance loss remains unchanged but the dipole polarization loss induced by them weakens. Obviously, it is inconsistent with the growing ϵ_p'' (Fig. 3b). Assuming dipole polarization predominantly governs polarization loss across microscales and significantly boosts EWA, exemplary reflection loss values would be anticipated at 600 °C. However, despite obtaining diverse designs for morphology and multi-shell structure, it is almost impossible for those 600 °C samples with high hetero-element content to lose EWA to less than -10 dB (Supplementary Fig. S48 and Supplementary Data 1). Therefore, the contribution from functional groups and impurity elements to the dielectric mechanism can be eliminated, and further confirm that the polarization loss mainly originates from the electron-rich graphite microcrystals obtained by sp^2 hybridization. According to the decomposition curve of the attenuation constant, electromagnetic wave attenuation caused by interface polarization is remarkable at 700 °C (Supplementary Fig. S49). In comparison, the proportion of electromagnetic wave attenuation caused by electrical conductance loss increases significantly at 1000 °C, due to the more extensive and continuous sp^2 domains (Supplementary Fig. S50 and Table S6). These results suggest that dielectric features decided by atomic configurations accumulate multiple times during structural modulation and are eventually passed to the overall performance.
2. Multi-shell SISB structures amplify the discrete sp^2 domain-induced interfacial polarization by improving the electron distribution and local electric field strength. Firstly, Raman spectroscopy shows that morphological parameters do not directly change the sp^2/sp^3 hybridization state (Supplementary Figs. S51, S52). Then, we compute the differential electron density compared to no electric field state by applying electric fields to same sp^2 - sp^3 hybridization models. Results revealed a pronounced charge imbalance between conjugated and non-conjugated regions. Enhanced electron gain/loss along the field direction in nonconjugated areas modulates the charge populations of sp^3 -C atoms, subsequently augmenting the electrostatic potential at the conjugate-nonconjugated interface perpendicular to the field direction (Supplementary Fig. S53). In essence, this local field modulation introduces new dipole moments and amplifies preexisting ones, thus improving the polarization of the whole system. This is directly reflected in solid samples. As curvature decreases and the electric field increases, the real/imaginary part (i.e., energy storage/loss) and $\tan\delta$ increase (Supplementary Fig. S54). Although less pronounced than in multi-shell SISB structures, this observation underscores the alteration of intrinsic dielectric properties by nano-curvature-induced field effects. Furthermore, we perform COMSOL Multiphysics simulations (Supplementary Figs. S55–S59). At a given frequency of 10 GHz, the group of bowl-shaped and short-chained hollow centers

exhibits a more pronounced electric field response and enhances it with the increase in the number of shell layers. It is worth noting that, unlike the SIS morphology, the multi-shell structure does not change the orientation of the electric field distribution, but only amplifies the electric field in situ on a single-shell basis. The degree of amplification is influenced by the central symmetry of the morphology (short-chained hollow <bowl-shaped hollow <porous hollow <hollow). For instance, the most asymmetrical double-shell short-chain hollow outperforms other triple-shell configurations. These results suggest that the increase in the local electric field is similarly influenced by the underlying basic unit, akin to the previously mentioned inheritance of dielectric characteristics.

Based on the above, the accumulated charge imbalances at multiple scales, combine to produce a collective behavior of interlocking and cross-scale dielectric loss. Cascade effects between discrete sp^2 domains and multi-shell SISB structures promote multiple iterations of polarization loss, thus enabling amorphous systems to operate efficiently and deplete electromagnetic waves.

EWA performance and electromagnetic application

The EWA performance of different continuum medium models (20, 25, and 30 wt%) is calculated through transmission line theory, and K-Means clustering was performed to draw a circular hotspot map (Fig. 5a). A large number of experimental samples help to observe the effectiveness of cascade effect by macro statistics. The statistical results indicate that: 1) superior EAB is always achieved at 700 °C, validating that the conjugate-nonconjugate interface polarization induced by discrete graphite microcrystals in amorphous carbon favors broadband absorption; 2) the performance of the multi-shell SISB structure is particularly prominent under low-filling conditions. Especially for 20 wt%, the relationship between morphology and EAB generally follows the trend of multi-shell SISB structure > multi-shell SIS structure > non-multi-shell structure. Previously, the success of Maxwell electromagnetics in the continuum model tells us that high-filling ratios can form macroscopic conductive pathways and increase $\epsilon_c''^{4,42}$. This sacrifices impedance matching at low and medium frequencies, resulting in counterproductive effects (Supplementary Fig. S60). Interestingly, the strongly polarized nature of multi-shell SISB samples (700 °C) dictates that it does not rely on optimizing dielectric loss through high-filling. On the contrary, these samples can demonstrate their polarization ability more independently through a diluted continuous medium model, which is more powerful than simply increasing the medium concentration (Supplementary Fig. S61 and Table S7). The EWA performance of amorphous nanostructures successfully demonstrates the importance of cascade effects on amorphous EWA materials (Fig. 5b).

We discuss separately the two groups of multi-shell SISB samples that achieved excellent EWA. At 700 °C and 20 wt%, both the triple-shell bowl-shaped hollow PRNs (mbh-PRNs-2) and double-shell short chain-shaped hollow PRNs (dch-PRNs) derived carbon achieve full coverage of X-band and Ku-band in a wide range of thickness (Fig. 5c–f), meaning slight thickness errors are allowed in the production operation. Notably, mbh-PRNs-2 (700 °C, 20 wt%) achieved a maximum EAB of 8.17 GHz and a minimum reflection loss (RL_{\min}) of -37.88 dB, while dch-PRNs-2 (700 °C, 20 wt%) achieved a maximum EAB of 8.17 GHz and an RL_{\min} of -37.88 dB. Based on the metal back-plane model, the incident wave is reflected multiple times between the surface of the dallenbach layer and the metal bottom surface. When an electromagnetic wave is reflected back with an odd number of half wavelengths, the opposite phases of the waves lead to interference phase extinction. As a result, peaks of the reflection loss curves for a given thickness fall on the 1/4 wavelength curves (Supplementary Fig. S62a–d). On the other hand, for a given material, its thickness,

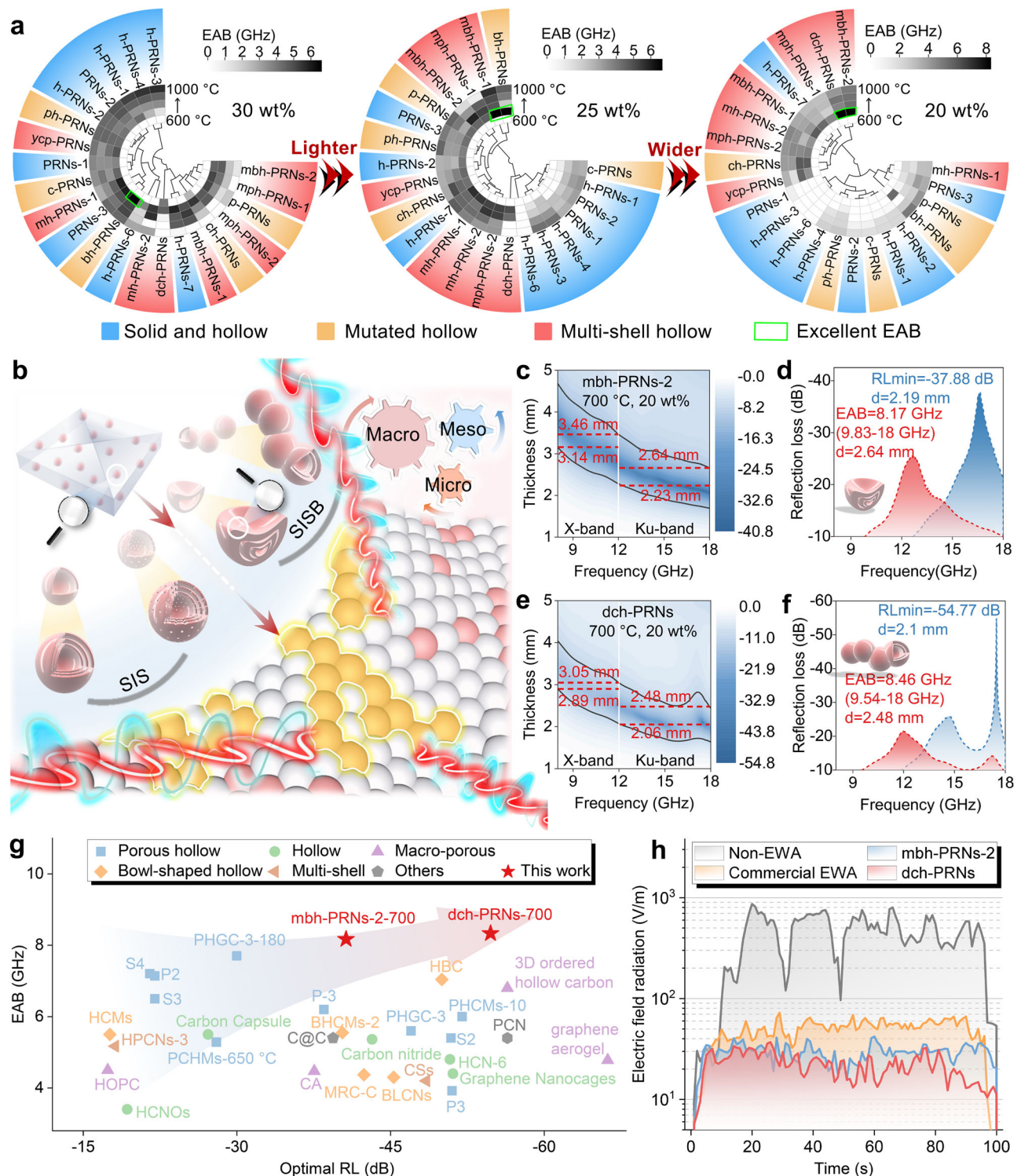


Fig. 5 | EWA performances of amorphous carbon. **a** The ring-shaped thermograms of the effective absorption bandwidth for different filling rates, pyrolysis temperatures, and morphologies. Use the K-Means algorithm to data analysis. **b** Schematic representation of the EWA cascade effect. Dielectric features initially determined by atomic configuration are realized to accumulate during the stepwise modulation of nano-curvature, structural asymmetry, and multi-shell structure, which are inherited to the final dielectric loss properties. The interlocking, rather than cumulative, effects of microscopic, mesoscopic, and macroscopic multiscale

factors achieve efficient EWA. **c** 2D EWA performance plot of triple-shell bowl-shaped hollow PRNs (mbh-PRNs-2, 700 °C, 20 wt%). **d** The widest EAB and the strongest reflection loss of mbh-PRNs-2 (700 °C, 20 wt%). **e** 2D EWA performance plot of double-shell short chain-shaped hollow PRNs (dch-PRNs, 700 °C, 20 wt%). **f** The widest EAB and the strongest reflection loss of dch-PRNs (700 °C, 20 wt%). **g** Compared with the EWA performance of other carbon materials with special structures in recent years. **h** The radiation value detected by electronic communication equipment under different circumstances.

frequency, and electromagnetic parameters together determine the normalized input impedance (Z_{in}). As can be observed from the Smith's image consisting of the real and imaginary parts of the complex Z_{in} (Supplementary Fig. S62e, f), the closer the real part is to 1 the closer the imaginary part is to 0, meaning that RL_{min} will be smaller. For EAB, broadband absorption is triggered when Z_{in} values at more frequencies fall in the effective range. Apparently, a unique physical mechanism is triggered by the synergistic regulation of phenolic multiple dynamics and discrete crystallization thermodynamics to obtain suitable dielectric parameters. Therefore, our multi-shell SISB structure amorphous carbon has advanced EWA properties (Fig. 5g and Supplementary Table S8), compared with other carbon materials with special structures (e.g., porous hollow, hollow, macro-porous, bowl-shaped hollow, yolk-shell, etc.).

In addition, their strong electromagnetic radiation loss characteristics are verified by a three-dimensional visualization image of the radar scattering cross section (RCS) (Supplementary Fig. S63). The RCS value is usually largest in the vertical direction, so the RCS value at 0° is used to represent the bottom line of absorption. As we expected, the trend of the RCS value at dynamic frequency corresponds exactly to the reflection loss curve (Supplementary Fig. S64). The electromagnetic stealth achieved by the perfect electron conductor model after the application of an absorbing layer is almost at the same level as that of birds²⁰. Such a result gives us confidence and drives us to explore the application value.

Our multi-shell SISB amorphous carbon material, in addition to its excellent EWA performance, offers the advantages of phenolic-derived carbon, such as light weight, low price, thermally stable, chemically stable and easy to process. We consider making it into an EWA patch for communication equipment (Supplementary Fig. S65). 20 wt% mbh-PRNs-2 (700 °C) and dch-PRNs (700 °C) are homogeneously mixed with 80 wt% fluoroelastomer, respectively, and acetone is used as a co-solvent. No processing problems such as agglomeration or settling occur throughout the process. After evaporation of the acetone in a specific mold at room temperature, a 2 mm thick flexible EWA patch has been formed. The patch is placed on the surface of the radiation source of the communication device. A radiation detection device is placed at a distance of 5 cm from the communication equipment and real-time radiation values are recorded to verify the effectiveness of the material in suppressing electromagnetic radiation. As shown in Fig. 5h, the exposed equipment has a very high radiation value of 10^3 V/m. When the equipment is attached to commercial EWA material, it is lower than 60 V/m. When the equipment is attached to our amorphous carbon patch, it is even less than 40 V/m. It is obvious that our materials have great application potential in resisting electromagnetic radiation and maintaining physiological health.

Discussion

In a word, we develop an amorphous nanostructure platform with high spatial dimensional diversity, linking cross-scale mechanisms with macroscopic behavior. The platform is constructed through multiple kinetic dynamics (phenolic growth kinetics, ethanol-modified growth kinetics, inflation-deflation dynamics, interfacial polymerization dynamics), as well as a multi-shelling strategy based on the Layer-By-Layer process. Hundreds of sets of amorphous carbon samples are obtained by thermodynamic conditioning and their complex collective behavior of EWA is investigated at compartmentalized scales, thus revealing the cascade effect. This effect runs through the entire system from atomic configuration to nano interface and micromorphology, promoting the application of dielectric polarization in promising electromagnetic protection. We hope that this methodology of amorphous nanostructures and the interpretation of cross-disciplinary and cross-scale cascade effects will extend the feasibility of amorphous science in material research.

Methods

General

The electromagnetic performance experimental, electromagnetic radiation detection experiment, DFT, RCS, and COMSOL Multiphysics simulations are given in the Supplementary Methods.

Preparation of phenolic resin nanoparticles (PRNs) and chain PRNs (c-PRNs)

To prepare the yellow powder, 0.1 g of 3-aminophenol and 0.1 ml of ammonia were dissolved in 30 ml of deionized water. The solution was stirred for 5 minutes. Next, 0.1 ml of formaldehyde solution was added to the mixture, which was then stirred using an electromagnetic stirrer for 30 min. The solution was then centrifuged at a speed of 10,000 rpm to separate the supernatant, leaving behind a yellowish precipitate. The precipitate was then re-dispersed in a suitable amount of deionized water using a numerical control ultrasonic device operating at 40 KHz and 100 W. This process of centrifugation ($7104 \times g$) and ultrasonic treatment was repeated three times. Afterward, the precipitate was dried overnight in a vacuum oven, resulting in the formation of a yellow powder. This powder was ground and labeled as PRNs. To differentiate between different temperature conditions, samples with liquid phase temperatures of 10 °C, 20 °C, and 30 °C were labeled as PRNs-1, PRNs-2, and PRNs-3, respectively. Additionally, samples with 0.05 ml and 0.2 ml of ammonia were labeled as PRNs-4 and PRNs-5. Samples without ultrasonic treatment were marked as c-PRNs.

Preparation of hollow PRNs (h-PRNs), bowl-shaped hollow PRNs (bh-PRNs), and chain hollow PRNs (ch-PRNs)

0.1 g of 3-aminophenol and 0.1 ml ammonia were dissolved in 30 ml deionized water and stirred for 5 min. The 0.1 ml formaldehyde solution was added to the mixed solution and the 30 min was stirred by electromagnetic stirring. Added acetone to dissolve the low molecular weight nuclei in the central area and stirred for 30 min. Centrifugation ($7104 \times g$) and ultrasonic dispersion were carried out for three times with the same parameters. The powder obtained by drying and grinding was h-PRNs. The products obtained with acetone volumes of 10 ml, 15 ml, 20 ml, 30 ml, and 40 ml were marked as h-PRNs-x, $x = 1, 2, 3, 4$, and 5. It should be noted that the production of h-PRNs-5 is so small that it is not possible to collect enough powder for vacuum pyrolysis and test electromagnetic properties.

After adding acetone, the centrifuged sample of 15 min was marked as bh-PRNs. After adding acetone, the sample treated by centrifugation ($7104 \times g$) 30 min and ultrasonic treatment by 20 KHz was marked as ch-PRNs.

Preparation of porous PRNs (p-PRNs) and porous hollow PRNs(ph-PRNs)

0.1 g 3-aminophenol and 0.1 ml ammonia were dissolved in 20 ml deionized water and 10 ml ethanol to stir for 5 min. 0.1 ml formaldehyde solution was added to the mixture and 30 min was stirred. The samples that were not treated with acetone and those that were treated with acetone were labeled as p-PRNs and ph-PRNs, respectively.

Preparation of multi-shell PRNs, e.g., multi-shell hollow PRNs (mh-PRNs-1 and mh-PRNs-2), multi-shell porous hollow PRNs (mph-PRNs-1 and mph-PRNs-2), and multi-shell bowl-shaped hollow PRNs (mbh-PRNs-1 and mbh-PRNs-2)

Before the second round of synthesis, the powder obtained in the first round was dispersed in a mixed solution of 3-aminophenol and ammonia. The mass of the raw material and the volume of the solution are 1.5 times that of the previous round. Except for the chain-like structure, all the other groups need to be treated by 40 KHz. Then, the

30 min reaction was carried out by dropping 1.5 times of formaldehyde solution. After the phenolic Polycondensation reaction is completed, acetone with the same volume as the solution is added, waiting for 30 min (bowl-shaped structure only needs 15 min), and then centrifuged. If the target structure is a three-layer shell, you need to repeat the operation again. The mass/volume of the raw materials synthesized in the third round is 1.5 times as much as that in the second round.

Preparation of a series of amorphous carbon

Place the phenolic precursor powder obtained above in a crucible and conduct high-temperature pyrolysis in an environment filled with argon gas. Raise the temperature from room temperature to the target annealing temperature (600, 700, 800, 900, and 1000 °C) at a heating rate of 5 °C per minute for 2 hours, and then naturally cool to room temperature. The obtained samples need to be ground. The annealing temperature is used as a parameter to distinguish the samples, for example, PRNs 1 was marked as PRNs 1-600 after carbonization at 600 °C.

Characterization

Surface structures were obtained by surface scanning in field emission scanning electron microscope (FE-SEM, Hitachi, S-4800) mode, respectively. Dynamic light scattering (DLS, Mastersizer 2000) was used to test the average particle size. The high-resolution local structure, selected area electron diffraction (SAED), and element mapping were got by a double spherical aberration-corrected transmission electron microscope (TEM, Spectra 300). N₂ adsorption-desorption curves were got by a chemisorption analyzer (V-Sorb X800). The vacancy defect information was got by EPR (MS-5000, 25 mW, 10.2 GHz). The electron-hole recombination rate of samples was got by PL (Varioskan LUX). The Phase composition and crystal structure were got by XRD (ARL EQUINOX 3000, $\lambda = 0.15418$ nm) and Raman (HR-TEC-785, $\lambda = 532$ nm). The thermodynamic regulation parameters of phenolic are based on the test results of in situ thermogravimetry-differential scanning calorimetry (Tg-DSC) in nitrogen. The functional groups were obtained by FT-IR spectroscopy (Nicolet iS5). The valence of the elements on the surface of the sample is determined by XPS (Thermo Kalpha, Al K $\alpha = 1486.6$ eV). The EIS of samples was obtained by an electrochemical workstation (CS310H). In the test, the counter electrode (Pt plate), reference electrode (Ag/AgCl), and electrolyte (3.5 wt% NaCl) were selected. The molecular weight of ethanol solution PRNs was determined by liquid chromatography-mass spectrometry (LC-MS, Agilent 1260). The molecular weight of PRNs was measured by GPC. The surface electronegativity was obtained by Zeta potential tester (JS94HM, the liquid is deionized water). The chemical composition and physical properties of the samples were analyzed with the aid of solid-state nuclear magnetic resonance (ssNMR). The resistivity was measured by the four-probe method.

Data availability

All data needed to evaluate the conclusions in the paper are presented in the paper and/or the Supplementary Information. Additional data related to this paper may be requested from the authors. Source data are provided with this paper.

References

- Liu, L. et al. Specific electromagnetic radiation in the wireless signal range increases wakefulness in mice. *Proc. Natl Acad. Sci. USA*. **118**, e2105838118 (2021).
- Iqbal, A. et al. Anomalous absorption of electromagnetic waves by 2D transition metal carbonitride Ti₃CNT_x (MXene). *Science* **369**, 446–450 (2020).
- Butler, K. T. et al. Machine learning for molecular and materials science. *Nature* **559**, 547–555 (2018).
- Xiao, H. et al. An invertible, invariant crystal representation for inverse design of solid-state materials using generative deep learning. *Nat. Commun.* **14**, 7027 (2023).
- Zhao, Z. et al. Advancements in microwave absorption motivated by interdisciplinary research. *Adv. Mater.* **36**, 2304182 (2024).
- Lee, D. et al. Data-driven design for metamaterials and multiscale systems: a review. *Adv. Mater.* **36**, 2305254 (2024).
- Lan, S. et al. A medium-range structure motif linking amorphous and crystalline states. *Nat. Mater.* **20**, 1347–1352 (2021).
- Joo, W.-J. et al. Realization of continuous Zachariasen carbon monolayer. *Sci. Adv.* **3**, e1601821 (2017).
- Lu, H. When physics meets chemistry at the dynamic glass transition. *Rep. Prog. Phys.* **87**, 032601 (2024).
- Li, N. et al. Fullerene fragment restructuring: how spatial proximity shapes defect-rich carbon electrocatalysts. *J. Am. Chem. Soc.* **145**, 24580–24589 (2023).
- Shang, Y. et al. Ultrahard bulk amorphous carbon from collapsed fullerene. *Nature* **599**, 599–604 (2021).
- Toh, C.-T. et al. Synthesis and properties of free-standing monolayer amorphous carbon. *Nature* **577**, 199–203 (2020).
- Wang, Q. et al. Highly conductive nitrogen-doped sp²/sp³ hybrid carbon as a conductor-free charge storage host. *Adv. Funct. Mater.* **32**, 2209201 (2022).
- Li, Z. et al. Ultrastrong conductive in situ composite composed of nanodiamond incoherently embedded in disordered multilayer graphene. *Nat. Mater.* **22**, 42–49 (2023).
- Tian, H. et al. Disorder-tuned conductivity in amorphous monolayer carbon. *Nature* **615**, 56–61 (2023).
- Ding, J. et al. Sulfur-grafted hollow carbon spheres for potassium-ion battery anodes. *Adv. Mater.* **31**, 1900429 (2019).
- Lei, L. et al. Carbon hollow fiber membranes for a molecular sieve with precise-cutoff ultramicropores for superior hydrogen separation. *Nat. Commun.* **12**, 268 (2021).
- Han, F. et al. On demand synthesis of hollow fullerene nanostructures. *Nat. Commun.* **10**, 1548 (2019).
- Tian, Q. et al. Mesoporous carbon spheres with programmable interiors as efficient nanoreactors for H₂O₂ electrosynthesis. *Nat. Commun.* **15**, 983 (2024).
- Tao, J. et al. Catfish effect induced by anion sequential doping for microwave absorption. *Adv. Funct. Mater.* **33**, 2211996 (2023).
- Chen, Y. et al. Defect-selectivity and “Order-in-Disorder” engineering in carbon for durable and fast potassium storage. *Adv. Mater.* **34**, 2108621 (2022).
- Zhang, Z. et al. Hollow multihole carbon bowls: a stress-release structure design for high-stability and high-volumetric-capacity potassium-ion batteries. *ACS Nano* **13**, 11363–11371 (2019).
- Liang, J. et al. Complex hollow bowl-like nanostructures: synthesis, application, and perspective. *Adv. Funct. Mater.* **31**, 2007801 (2021).
- Liu, P. et al. Hollow engineering to Co@N-doped carbon nanocages via synergistic protecting-etching strategy for ultrahigh microwave absorption. *Adv. Funct. Mater.* **31**, 2102812 (2021).
- Tao, J. et al. Selective coding dielectric genes based on proton tailoring to improve microwave absorption of MOFs. *Adv. Powder Mater.* **2**, 100091 (2023).
- Tao, J. et al. Multi-shell hollow porous carbon nanoparticles with excellent microwave absorption properties. *Carbon* **172**, 542–555 (2021).
- Zhang, H. et al. Highly selective nano-interface engineering in multishelled nanocubes for enhanced broadband electromagnetic attenuation. *Adv. Funct. Mater.* **34**, 2313829 (2024).
- Liu, J. et al. Hollow multi-shell SiC@C@PANI nanoparticles with broadband microwave absorption performance. *Appl. Surf. Sci.* **613**, 156098 (2023).

29. Zhang, X. et al. Tunable high-performance microwave absorption of Co_{1-x}S hollow spheres constructed by nanosheets within ultralow filler loading. *Adv. Funct. Mater.* **28**, 1800761 (2018).
30. Li, X. et al. Self-assembly core-shell graphene-bridged hollow MXenes spheres 3D foam with ultrahigh specific EM absorption performance. *Adv. Funct. Mater.* **28**, 1803938 (2018).
31. Song, S. et al. Universal scaling law of glass rheology. *Nat. Mater.* **21**, 404–409 (2022).
32. Xia, Y. et al. A review on graphene-based electromagnetic functional materials: electromagnetic wave shielding and absorption. *Adv. Funct. Mater.* **32**, 2204591 (2022).
33. Fan, R. et al. Constructing metastructures with broadband electromagnetic functionality. *Adv. Mater.* **32**, 1904646 (2020).
34. Tang, Z. et al. Synthesis of CuCo_2S_4 @Expanded Graphite with crystal/amorphous heterointerface and defects for electromagnetic wave absorption. *Nat. Commun.* **14**, 5951 (2023).
35. Zhang, C. et al. Unveiling the sp^2 - sp^2 C-C polar bond induced electromagnetic responding behaviors by a 2D N-doped carbon nanosheet absorber. *Adv. Sci.* **11**, 2306159 (2024).
36. Yu, Z.-L. et al. Revitalizing traditional phenolic resin toward a versatile platform for advanced materials. *Acc. Mater. Res.* **5**, 146–159 (2024).
37. Pi, Y. et al. Multilevel hollow phenolic resin nanoreactors with precise metal nanoparticles spatial location toward promising heterogeneous hydrogenations. *Adv. Mater.* **34**, 2205153 (2022).
38. Yu, R. et al. Shaping nanoparticles for interface catalysis: concave hollow spheres via deflation-inflation asymmetric growth. *Adv. Sci.* **7**, 2000393 (2020).
39. Mohapatra, H. et al. Mechanically controlled radical polymerization initiated by ultrasound. *Nat. Chem.* **9**, 135–139 (2017).
40. Chen, G. et al. Ultrasonic field induces better crystallinity and abundant defects at grain boundaries to develop cus electromagnetic wave absorber. *Adv. Mater.* **35**, 2305586 (2023).
41. Wang, J. et al. Hollow multishelled structures for promising applications: understanding the structure-performance correlation. *Acc. Chem. Res.* **52**, 2169–2178 (2019).
42. Tao, J. et al. Ion-exchange strategy for metal-organic frameworks-derived composites with tunable hollow porous and microwave absorption. *Small Methods* **6**, 2200429 (2022).
43. Pan, F. et al. Sequential architecture induced strange dielectric-magnetic behaviors in ferromagnetic microwave absorber. *Adv. Funct. Mater.* **33**, 2300374 (2023).
44. He, G. et al. Microwave absorption of crystalline $\text{Fe/MnO}@C$ nanocapsules embedded in amorphous carbon. *Nano-Micro Lett.* **12**, 57 (2020).
45. Ding, J. et al. Boosted Interfacial Polarization from Multishell $\text{TiO}_2@Fe_3O_4$ @PPy Heterojunction for Enhanced Microwave Absorption. *Small* **15**, 1902885 (2019).
46. Wu, P. et al. Phase engineering on amorphous/crystalline $\gamma\text{-Fe}_2\text{O}_3$ nanosheets for boosting dielectric loss and high-performance microwave absorption. *Adv. Funct. Mater.* **34**, 2311983 (2024).
47. Tao, J. et al. Multi-field coupled motion induces electromagnetic wave absorbing property regeneration of elastomer in marine environment. *Adv. Funct. Mater.* **34**, 2310640 (2024).
48. Zhang, X. et al. Tip effect assisted high active sites for oxygen evolution reaction tuned using transition metals (Cr, Fe and Mo) doped with CoP. *J. Mater. Chem. A* **11**, 23270–23277 (2023).
49. Gao, Z. et al. Tailoring built-in electric field in a self-assembled Zeolitic Imidazolate Framework/MXene nanocomposites for microwave absorption. *Adv. Mater.* **36**, 2311411 (2024).

Acknowledgements

This work is supported by the National Natural Science Foundation of China (52172091 to Z.Y., 52172295 to J.Z., 62104110 to J.W.); Defense Industrial Technology Development Program (JCKY2023605C002 to J.Z.); Frontier Leading Technology Basic Research Major Project of Jiangsu Province (BK20232013 to J.Z.); the Postgraduate Research & Practice Innovation Program of Jiangsu Province (KYCX23_0371 to J.T.). We acknowledge the Center for Microscopy and Analysis at Nanjing University of Aeronautics and Astronautics for conducting TEM characterization. We acknowledge the support of Suzhou Laboratory.

Author contributions

J.T. conceived and designed the experiments. J.Z., H.H. and Z.Y. supervised the project. J.T., K.Z. and X.T. performed experiments and acquired data. J.T., L.X. and H.W. analyzed the data. J.T. drafted the manuscript. J.W. performed the first-principles density functional theory simulation. All authors contributed to data interpretation, discussions, and manuscript preparation.

Competing interests

The authors declare no competing interests.

Additional information

Supplementary information The online version contains supplementary material available at <https://doi.org/10.1038/s41467-024-54770-5>.

Correspondence and requests for materials should be addressed to Jintang Zhou, Hongjing Wu, Jin Wang, Hexia Huang or Zhengjun Yao.

Peer review information *Nature Communications* thanks Yi Huang, Qiangchun Liu and the other, anonymous, reviewer(s) for their contribution to the peer review of this work. A peer review file is available.

Reprints and permissions information is available at <http://www.nature.com/reprints>

Publisher's note Springer Nature remains neutral with regard to jurisdictional claims in published maps and institutional affiliations.

Open Access This article is licensed under a Creative Commons Attribution-NonCommercial-NoDerivatives 4.0 International License, which permits any non-commercial use, sharing, distribution and reproduction in any medium or format, as long as you give appropriate credit to the original author(s) and the source, provide a link to the Creative Commons licence, and indicate if you modified the licensed material. You do not have permission under this licence to share adapted material derived from this article or parts of it. The images or other third party material in this article are included in the article's Creative Commons licence, unless indicated otherwise in a credit line to the material. If material is not included in the article's Creative Commons licence and your intended use is not permitted by statutory regulation or exceeds the permitted use, you will need to obtain permission directly from the copyright holder. To view a copy of this licence, visit <http://creativecommons.org/licenses/by-nc-nd/4.0/>.

© The Author(s) 2024